WS2-Induced Enhanced Optical Absorption and Efficiency in Graphene/Silicon Heterojunction Photovoltaic Cells

Journal:	*Nanoscale*
Manuscript ID	NR-ART-04-2018-003194.R2
Article Type:	Paper
Date Submitted by the Author:	03-Sep-2018
Complete List of Authors:	Debbarma, Rousan; University of Illinois at Chicago, Chemical Engineering Behura, Sanjay; University of Illinois at Chicago, Chemical Engineering Wen, Yu; University of Illinois at Chicago, Chemical Engineering Che, Songwei; University of Illinois at Chicago, Chemical Engineering Berry, Vikas; University of Illinois at Chicago, Department of Chemical Engineering

SCHOLARONE™
Manuscripts

WS$_2$-Induced Enhanced Optical Absorption and Efficiency in Graphene/Silicon Heterojunction Photovoltaic Cells

Rousan Debbarma, Sanjay K. Behura*, Yu Wen, Songwei Che, and Vikas Berry*

Department of Chemical Engineering, University of Illinois at Chicago, 810 S. Clinton Street, Chicago, IL 60607, United States

*Corresponding authors. E-mail: vikasb@uic.edu; sbehura1@uic.edu.

Abstract

The Van Hove singularity (VHS) induced enhancement of visible-frequency-absorption in atomically-thin two-dimensional (2D) crystals provides an opportunity for improved light management in photovoltaics; however, it requires the 2D nanomaterial to be in close vicinity to a photojunction. In this report, we design a Schottky junction-based photovoltaic system with single-layer graphene atop n-type silicon (n-Si), which is interfaced directly with few-layers of tungsten disulfide (WS$_2$) *via* a bottom-up CVD synthesis strategy. An enhanced power conversion efficiency in the architecture of WS$_2$-graphene/n-Si is observed compared to graphene/n-Si. Here, the WS$_2$ induced photon absorption, only one atom above the photo-junction enhanced short-circuit current density (J_{SC}), and the reconfiguration of the energy band structure led effective built-in electric field induced charge carrier transport (enhanced open-circuit voltage (V$_{OC}$)). Similar to graphene/n-Si Schottky junction, the WS$_2$-graphene/n-Si double junction exhibited non-linear current density-voltage (J-V) characteristics with a 4-fold increase in J_{SC} (2.28 mA/cm^2 in comparison to 0.52 mA/cm^2 for graphene/n-Si) and 40% increase in the V$_{OC}$ (184 mV compared to 130 mV for graphene/n-Si) with a 6-fold increase in the photovoltaic power conversion efficiency. Futuristically, we envision an evolution in 2D heterojunctions with sharp-transitions in properties within a few nanometers enabling control on optical-absorption, carrier-distribution, and band-structure for applications including tandem photovoltaic cells and 2D optoelectronic circuit-switches.

Keywords: 2D Nanomaterials, Van Hove Singularity, Raman, Heterojunction, Photovoltaics

1. INTRODUCTION

The abrupt gradients of optical and electronic properties within stacked van der Waals heterostructures of two-dimensional nanomaterials (2DNs) and heterojunctions of 2D crystals and bulk materials can be harnessed to achieve advanced functionalities.[1–5] The ultra-high charge carrier mobility and spectral transmittance of sp^2-hybridized graphene produced *via* catalytic chemical vapor deposition (CVD) process makes it an ideal candidate material for optoelectronic phenomena.[6–8] Typical CVD-produced graphene interfaced with lightly-doped silicon (n-Si) forms Schottky junction functioning as photovoltaic cells with illumination of light (air mass 1.5G).[9–11] Such heterojunctions show promising power conversion efficiency of >10% and further enhancement in the performance can be achieved by polymer doping of graphene with trifluoromethanesulfonic acid and also by using colloidal titanium dioxide (TiO_2) layer as an antireflective coating (ARC).[12,13]
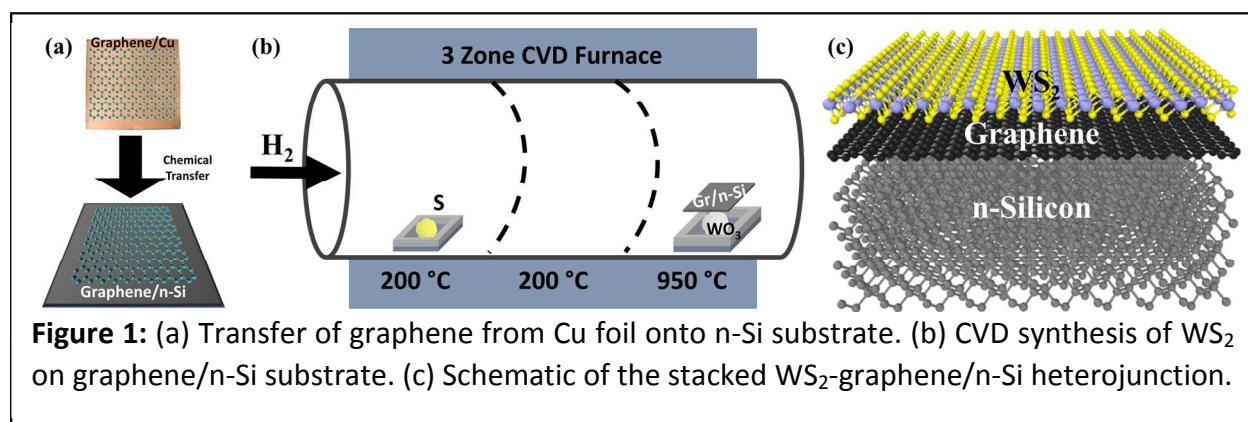
Atomically-thin transition metal dichalcogenides (TMDCs) exhibit strong light-matter interactions due to the Van Hove singularities (VHS) in the electronic density of states.[14] The Van Hove singularities in the density of states of TMDCs result in the sharp increase in the joint density of states in the visible region. This leads to an increased photo-absorption and electron-hole pair (exciton) generation in the visible range. In contrast, the Van Hove singularities in graphene's density of states lead to a pronounced absorption peak in the ultraviolet region.[15] Further, TMDCs of thickness less than 1 nm can absorb up to 5-10% of incident sunlight compared to 2-3% absorption in monolayer CVD graphene.[16,17] They also possess a finite and tunable band gap (1.4-2.1 eV) in the visible region and therefore they can absorb a broad range of the solar radiation spectrum (air mass 1.5G). Tungsten disulfide (WS_2) is a member of the layered group-VI TMDCs made up of covalently bonded S-W-S in-plane sheets held together *via* weak out-plane van der Waals forces.[18] The energy bandgap for WS_2 transitions from an indirect bandgap of 1.4 eV in its bulk to a direct bandgap of 2.1 eV in its monolayer form.[19] The chemical stability and the presence of only a weak impurity band compared to molybdenum disulfide (MoS_2),[2] makes WS_2 better suited as an active absorber material for applications in photovoltaics as the lack of impurity bands will lead to fewer electron-hole pair recombination. The CVD growth of single crystalline grains and large area WS_2 has been reported in the

literature.[20–22] CVD growth of TMDCs allows for a better control of the number of layers and helps realize clean interfaces by avoiding the use of polymer-based transfer techniques. The direct growth of WS_2 and other TMDCs *via* CVD will enable bulk production and eventually these 2DNs will find their way into commercial applications. A few reports have investigated utilizing WS_2 as a tunneling barrier in a graphene/WS_2/metal or graphene/WS_2/graphene vertical field-effect transistors (FETs) using mechanically exfoliated WS_2 films.[2,23] In another report, CVD grown WS_2 were transferred onto CVD grown graphene to investigate the interfacial doping effect of WS_2 on graphene.[24]
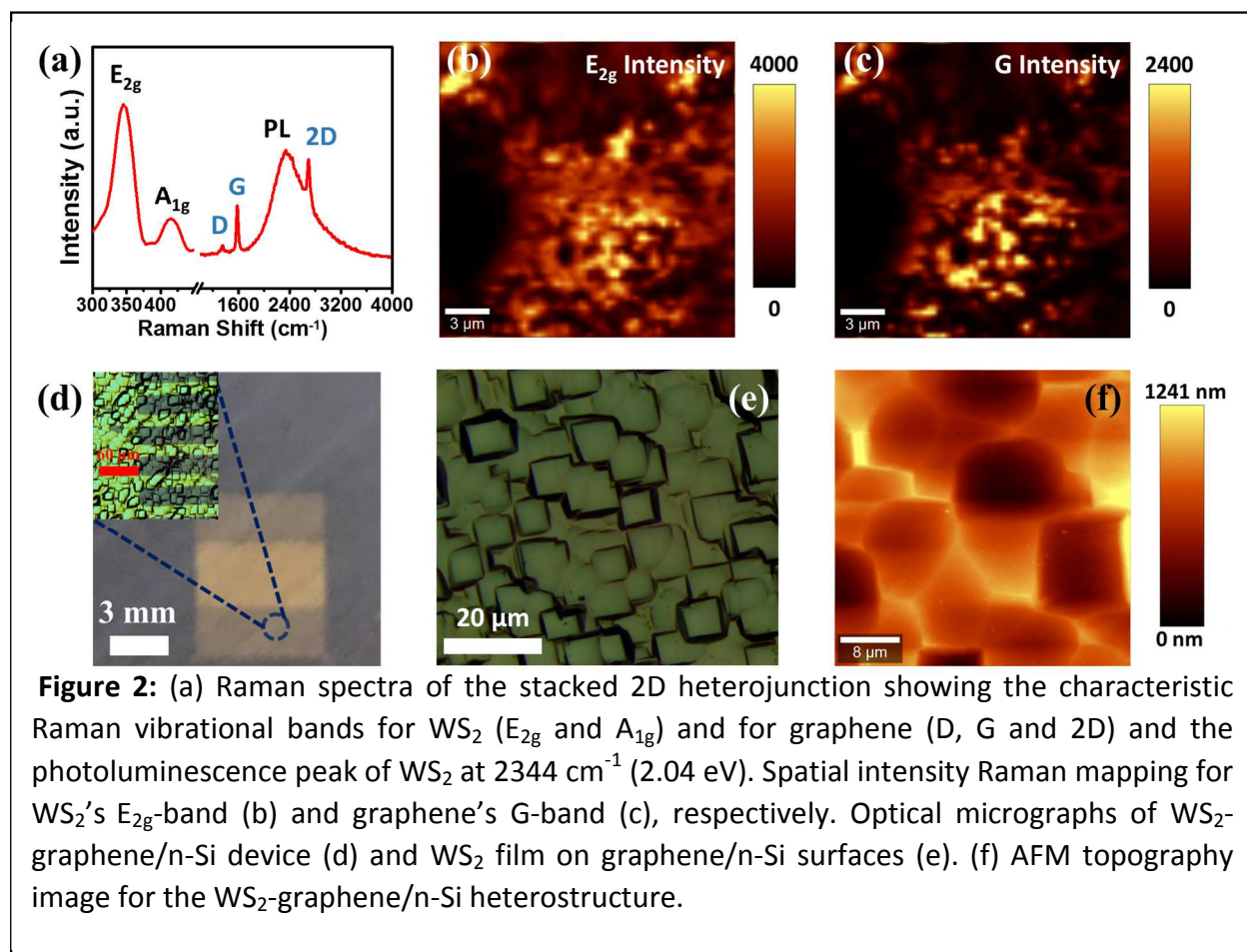
In this report, we show (a) the direct CVD growth of WS_2 on graphene *via* bottom-up CVD synthesis strategy (shown for the first time), (b) the development of a double junction photovoltaic cell by vertically stacking WS_2 on graphene on n-type Si substrate, and (c) an enhanced power conversion efficiency (PCE) in WS_2-graphene/n-Si photovoltaic solar cells over graphene/n-Si single Schottky junction solar cells. The mechanism of efficiency-enhancement is attributed to energy band restructuring, enhanced photon absorption, exciton generation and dissociation, and built-in electric field induced transport across the double junction.

2. RESULTS AND DISCUSSION

The bottom-up synthesis strategies for creating vertically-stacked WS_2-graphene/n-Si dual-junction nano-architecture is presented in Figure 1. Here a single-layer of CVD-produced graphene film on copper (Cu) foil is chemically transferred *via* carrier-film method onto a heavily-textured and lightly-doped solar-grade n-Si (100) substrate (Figure 1a) followed by the growth of atomically-thin WS_2 layers (Figure 1b) *via* vapor-transport based low-pressure thermal CVD technique.[25] As shown in Figure 1b, the WS_2-graphene/n-Si structures were

Figure 1: (a) Transfer of graphene from Cu foil onto n-Si substrate. (b) CVD synthesis of WS_2 on graphene/n-Si substrate. (c) Schematic of the stacked WS_2-graphene/n-Si heterojunction.

prepared by growing WS_2 on the graphene/n-Si substrates in a three zone CVD furnace with a one inch quartz tube. As shown in Figure 1b, the graphene/n-Si samples were inverted and placed on top of a crucible containing 10 mg of WO_3 powder at the third zone of the furnace and sulfur powder was kept in the first zone in a quartz boat. The CVD reaction chamber was vacuumed to 2 mTorr in 20 minutes and then a steady flow of 50 sccm of H_2 was maintained throughout the process. After a pressure of 220 mTorr was stabilized, the first and the second zones were heated to 200 °C and the third zone was heated to 950 °C in 30 minutes. The temperatures in all the three zones were held for the next 30 minutes. After 30 minutes, the chamber was cooled down to 700 °C at the rate of ~2 °C/min. This was followed by fast cooling (~100 °C/min) of the chamber to room temperature. Details of the CVD synthesis of graphene on catalytic Cu foil, its chemical transfer onto n-Si substrates are provided in the Materials and Methods section. In this work, ten different WS_2-graphene/n-Si samples were produced *via* the CVD process. The synthesized vertically stacked heterojunction of WS_2-graphene/n-Si (Figure

Figure 2: (a) Raman spectra of the stacked 2D heterojunction showing the characteristic Raman vibrational bands for WS_2 (E_{2g} and A_{1g}) and for graphene (D, G and 2D) and the photoluminescence peak of WS_2 at 2344 cm^{-1} (2.04 eV). Spatial intensity Raman mapping for WS_2's E_{2g}-band (b) and graphene's G-band (c), respectively. Optical micrographs of WS_2-graphene/n-Si device (d) and WS_2 film on graphene/n-Si surfaces (e). (f) AFM topography image for the WS_2-graphene/n-Si heterostructure.

1c) is elucidated by Raman spectroscopy. The spectrum for the stacked heterojunction shown in Figure 2a exhibits the signature Raman vibrational modes for WS_2 (in-plane $E_{2g}/347$ cm^{-1} and out-plane $A_{1g}/415$ cm^{-1})[26] and graphene (D/1352 cm^{-1}, G/1584 cm^{-1} and 2D/2700 cm^{-1})[27] as well as the photoluminescence (PL) peak for WS_2 (2344 cm^{-1} or 2.04 eV). The presence of PL peak and a peak position difference of 68 cm^{-1} between the E_{2g} and A_{1g} peaks indicate that the WS_2 film grown on the graphene/n-Si substrate is few-layers thick and not bulk.[22,28] The presence of semi-metal graphene quenches the strong PL of WS_2.[29] Figure 2b shows the spatial mapping of the intensity of WS_2's E_{2g} peak, which represents the in-plane phonon mode involving the vibration of the metal (W) and the chalcogen (S) atoms.[30] The spatial mapping of the intensity of the graphene's G band (~1600 cm^{-1}), which represents the phonon mode for the in-plane stretching of carbon-carbon bond,[31] is shown in Figure 2c. A continuous coverage of WS_2 layer on the graphene transferred onto the n-Si substrate can be confirmed from the spatial mappings in Figures 2b and c. The variation in intensities in the spatial mapping is due to the surface texture of the underlying n-Si substrate, which is intentionally made on the n-Si substrate for enhanced light absorption.[32] Because of the surface texturing, some portion of the scanned area are above or below the focal plane used in the Raman measurement which ultimately leads to the variations in the intensities. The surface texture can also be seen in the micrographs and atomic force microscopy (AFM) topography image for the WS_2-graphene/n-Si device, which are shown in Figures 2d-2f.

Figures 3a and b show the dark current-voltage (*I-V*) characteristics of the graphene/n-Si and WS_2-graphene/n-Si heterojunction devices, respectively. Both devices have an active area of 0.1 cm^2. The *I-V* curves show non-linear diodic features for both the heterojunctions. The typical dark *I-V* relation[10,33] for a diode is given by:

$$I = I_O \left(exp \left(\frac{V - IR_S}{nV_T} \right) - 1 \right) \qquad (1)$$

where I_O is the reverse saturation current, R_s is the series resistance, n is the diode ideality factor and V_T is the thermal voltage ($V_T = \frac{k_B T}{q}$). The diode equation is generally for a single p-n junction diode. In our case, even though we have a double junction structure (WS_2-graphene/n-Si), the electron transport occurs from WS_2 to graphene and then to n-Si (explained later) and

so we can model the device as a single p-n junction diode and analyze the aforementioned parameters. The diode parameters for the dark *I-V* relation were determined by employing a non-linear implicit curve fitting. The ideality factors determined from the non-linear implicit fitting of the *I-V* curves are 2.78 and 20.6 for the graphene/n-Si and the WS$_2$-graphene/n-Si devices, respectively. A previous work involving gallium nitride (GaN) based heterojunction reported anomalously high ideality factors.[34] It has been shown that the rectification of the individual junctions in the heterojunction can lead to high ideality factors and the measured ideality factor is the sum total of the ideality factors of the individual junctions. Here both the
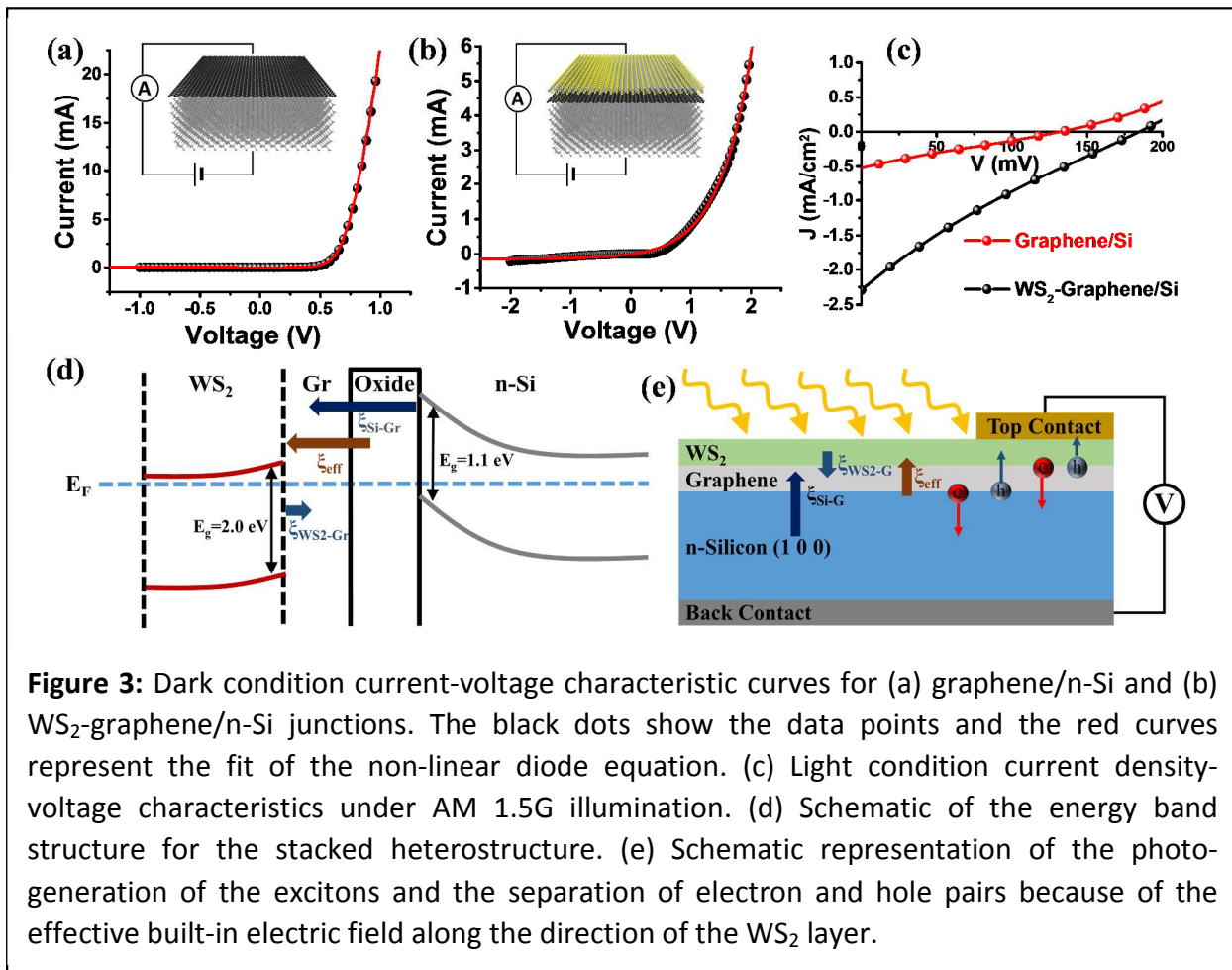
Figure 3: Dark condition current-voltage characteristic curves for (a) graphene/n-Si and (b) WS$_2$-graphene/n-Si junctions. The black dots show the data points and the red curves represent the fit of the non-linear diode equation. (c) Light condition current density-voltage characteristics under AM 1.5G illumination. (d) Schematic of the energy band structure for the stacked heterostructure. (e) Schematic representation of the photo-generation of the excitons and the separation of electron and hole pairs because of the effective built-in electric field along the direction of the WS$_2$ layer.

WS$_2$/graphene and graphene/n-Si junctions in the WS$_2$-graphene/n-Si structure contribute to the high ideality factor compared to just the one junction in the graphene/n-Si device.

The diode and photovoltaic parameters outlined in Table 1 shows that the addition of a thin film of WS_2 on graphene/n-Si structure leads to a four-fold increase in the short-circuit current density (J_{sc}) and the open-circuit voltage (V_{oc}) increases by 40%. This leads to a 6-fold improvement of the solar cell power conversion efficiency (η) from 0.015% to 0.1% *via* inclusion of a few layers of WS_2 on graphene/n-Si. The kink in the *J-V* curve (Figure 3c) can be attributed to the native oxide layer on the n-Si surface, which leads to an increased recombination current.[10] This results in low fill factors of 21% and 21.35% for the graphene/n-Si and the WS_2-graphene/n-Si devices, respectively. The large active area can also be attributed to the low fill factor, which contributes to the low efficiencies observed in our solar cell devices.[13] A further improvement in the performance of the WS_2-graphene/n-Si device can be achieved *via* (a) chemical or physical doping, (b) plasmonic enhancement *via* nanoparticle anchoring, (c) anti-reflection coating for improved light management, (d) improving isolation of electrodes, and (e) maximizing the optical absorption *via* the optimization of the number of WS_2 layers. To understand the increase in the short circuit current density and the open circuit voltage, we need to look into the electrostatics and energetics of the photo-junction interfaces.

The deposition of n-type WS_2 layers on graphene/n-Si leads to the formation of a double junction photovoltaic cell. Unlike a single p-n junction where electron transport is from the p-side to the n-side upon light absorption with photon energy higher than the bandgap of the junction material, the transport of electrons in the WS_2-graphene/n-Si is from the n-type WS_2 to p-type graphene and then to the n-Si side. This can be attributed to the stronger built-in electric field in the graphene/n-Si interface (ξ_{Si-G}) compared to the WS_2-graphene interface $\left(\xi_{WS_2-G}\right)$ as represented in Figures 3d and 3e. The electric field in the depletion region is directly proportional to the doping density and inversely proportional to the permittivity of the material. The built-in electric fields at the WS_2-graphene and graphene/n-Si interfaces can be modelled using the following equations:

$$\xi_{WS_2-G}(x) \approx \frac{qN_{D(x-W_n)}}{\varepsilon_{WS_2}\varepsilon_o} \tag{2}$$

$$\xi_{Si-G}(x) \approx \frac{qN_{D(x-W_n)}}{\varepsilon_{Si}\varepsilon_o}, \tag{3}$$

where x is the distance from the given interface, q $(1.6 \times 10^{-19} \, C)$ is the elementary charge, N_D is the intrinsic dopant concentration $(N_D[Si] \approx 10^{18} \, cm^{-3})$, W_n is the depletion region width, $\varepsilon_{WS_2} = 4.4 - 11.5$ (monolayer to bulk)[35] and $\varepsilon_{Si} = 11.68$ are the relative dielectric constants and ε_o $(\varepsilon_o = 8.85 \times 10^{-12} \, F/m)$ is the vacuum permittivity. The intrinsic doping concentration for WS$_2$ can be written as $N_D = \frac{N_S}{t}$ where N_S $(N_S \approx 10^9 \, cm^{-2})$ is the surface doping density and t is the WS$_2$ thickness.[36] The maximum electric field for both the junctions will be at the interface $(x = 0)$. The WS$_2$-graphene forms an abrupt 2D junction with no inter-diffusion and depletion region. In equation 2, the width of the depletion layer can be replaced by the thickness of the WS$_2$ layer, t. The depletion region width for the silicon-graphene junction can be expressed as:[37],

$$W_n = \sqrt{\frac{2\varepsilon_{Si}\varepsilon_o(V_{bi}-V_b)}{qN_D}}, \qquad (4)$$

where V_{bi} and V_b are the built-in and applied bias voltages, respectively. For V_{bi} = 0.5 V and V_b = 0 V, the depletion region width is $(W_n) \approx 0.01 \, \mu m$. Performing an order of magnitude analysis, we can show that $|\xi_{WS_2-G}(x = 0)| \approx 10^4 \, V/m$ and $|\xi_{Si-G}(x = 0)| \approx 10^7 \, V/m$ and so the electric field along the silicon-graphene direction is three orders of magnitude higher $\left(\frac{|\xi_{Si-G}(x=0)|}{|\xi_{WS_2-G}(x=0)|} \approx 10^3\right)$ than the electric field along the WS$_2$-graphene direction. As mentioned earlier, the presence of native oxide layer on the n-Si surface leads to a low fill factor of ~20%. This native oxide layer will also shield and make the net electric field weaker by a factor $(|\xi_{Si-G \, net}| = |\xi_{Si-G \, net}|/\varepsilon_{ox})$, which is the dielectric constant of the oxide layer (ε_{ox}). The oxide layer can be approximated to have the same dielectric constant as silicon dioxide $(\varepsilon_{ox} = 3.9)$. Therefore, the net electric field along the silicon-graphene direction is still of the order of $10^6 - 10^7 \, V/m$ and two to three orders of magnitude higher $\left(\frac{|\xi_{Si-G \, net}|}{|\xi_{WS_2-G}|} \approx 10^2 - 10^3\right)$ than the electric field in the WS$_2 \rightarrow$graphene direction. Once this electric field penetrates the WS$_2$ layer, it is further weakened by a factor given by the dielectric constant of WS$_2$ (ε_{WS_2}). Since WS$_2$ has a low dielectric constant, the net effective field $\xi_{Si-G \, net}$ in the WS$_2$ layers is still two to three orders of magnitude higher than ξ_{WS_2-G}. Therefore, despite the shielding of the

electric field by the native oxide layer and the opposing electric field in the $WS_2 \rightarrow$graphene direction, the relatively strong electric field in the n-Si$\rightarrow$graphene interface penetrates the atomically thin WS_2-graphene junction, and that leads to an effective electric field along the n-Si$\rightarrow WS_2$ direction. The effective field will drift the electrons towards n-Si and holes in the opposite direction towards WS_2.

Table 1: Diode equation parameters, short circuit current density, open circuit voltage, fill factors and the solar cell power conversion efficiencies for the two photovoltaic cells.

Photovoltaic Parameters	Graphene/n-Si	WS₂-graphene/n-Si
Dark Saturation Current, I_O (μA)	0.05	125
Series Resistance, R_s $(\Omega\text{-}cm^{-2})$	21.1	28.9
Ideality Factor, n	2.78	20.6
Short-Circuit Current, I_{sc} (mA/cm^2)	0.52	2.28
Open-Circuit Voltage, V_{oc} (mV)	130	184
Fill Factor, FF $(\%)$	21	21.3
Power Conversion Efficiency, η $(\%)$	0.015	0.1

The native n-type doping of WS_2 similar to that in MoS_2 can be attributed to sulfur vacancies.[38,39] It has been reported that on transferring WS_2 layer onto graphene surface, the WS_2 becomes less n-doped and the underlying graphene covered by the WS_2 becomes less p-doped *via* exchange of electrons.[24] However, for the direct CVD grown WS_2 on graphene, we observed the opposite trend. A higher n-doping is seen on WS_2 grown on graphene/n-Si compared to the WS_2 grown on SiO_2/Si surface. The increase in the doping level of WS_2 can be seen in the PL spectra shown in Figures 4a and 4b. The PL spectra for WS_2 on SiO_2 and on graphene/n-Si in Figure 4 have been deconvoluted using Lorentzian fitting into two different peaks representing the exciton emission (X) and the trion emission (X⁻).[40,41] The PL of WS_2 on graphene/n-Si shows a third peak that can be attributed to the 2D Raman vibrational mode for graphene. The blue-shift in the peak energy for the WS_2 on graphene compared to WS_2 on SiO_2 can be attributed to the structural imperfections and n-doping.[42] The two peaks have an energy
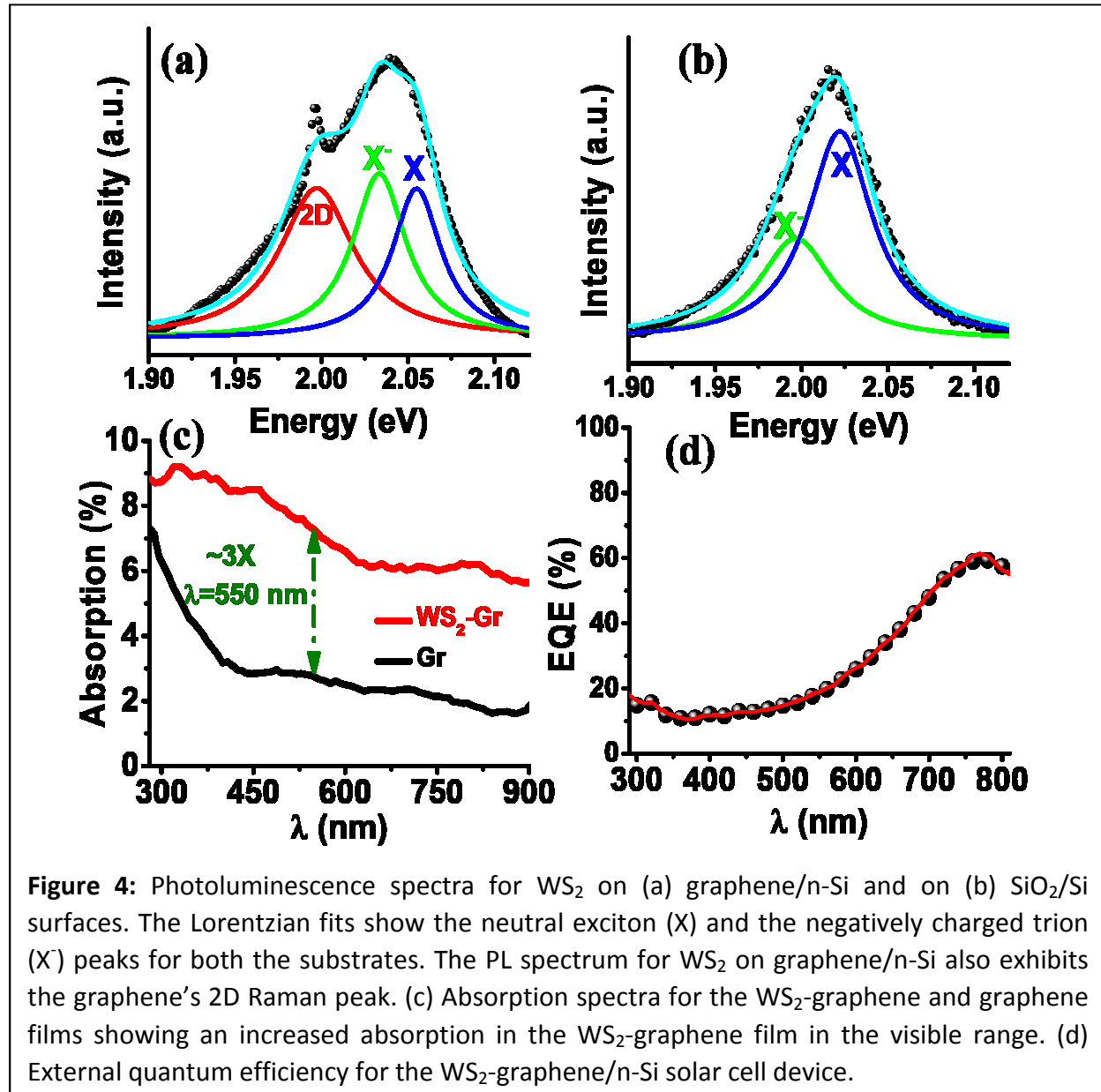
difference of 21.67 meV for WS_2 on graphene/n-Si and 25.55 meV for WS_2 on SiO_2 which is the sum of the trion binding energy and the fermi energy.[43–46] The intensity ratio of the trion emission peak to the exciton emission peak is higher for the WS_2 on graphene/n-Si $\left(\frac{I_{X^-}}{I_X} = 1.1\right)$ compared to that of WS_2 on SiO_2/Si $\left(\frac{I_{X^-}}{I_X} = 0.49\right)$ substrate. Further analysis is required to understand the increased trion concentration in direct growth of WS_2 on graphene. Although the PL analysis is not enough to confirm the doping effects on WS_2, the PL deconvolution and analysis does let us infer the ratio of trions to neutral excitons in the given system, which can be an indirect way of inferring the doping effect. The net negative charge of trions will aid in their drift under the effective in-built electric field towards the WS_2-graphene interface where they will dissociate into electrons and holes. The neutral excitons, due to the chemical potential difference, will diffuse both towards and away from the interface and they will eventually dissociate at the WS_2-graphene interface.

The open-circuit voltage (V_{oc}) of a solar cell is directly dependent on the built-in potential and parameters that affect the built-in voltage.[47] In the WS_2-graphene/n-Si device both the WS_2/graphene and graphene/n-Si junctions have built-in voltages that contribute to the V_{oc} of the device. In multi-junction solar cell devices, the V_{oc} increases with the number of additional junctions. It has been shown that the V_{oc} in multi-cell (tandem junctions) devices is close to the sum of the V_{oc} of single cells.[48–51] So the V_{oc} in the WS_2-graphene/n-Si device is the sum of the V_{oc} for WS_2-graphene and graphene/n-Si single junction devices. The presence of an extra junction in the WS_2-graphene/n-Si device leads to the increase in the V_{oc}.

The increase in the short circuit current density (J_{sc}) can be attributed to the higher light absorption coefficient of WS_2 compared to graphene.[14,16] The Van Hove singularities in the density of states of WS_2 leads to sharp increase in the joint density of states in the visible region (~2-3 eV) which ultimately corresponds to the improved photo-absorption and generation of excitons. In comparison, the Van Hove singularities in graphene results in the absorption peaks in the ultraviolet (UV) range. A 3-fold increase in the absorption in the visible range on deposition of WS_2 on top of graphene is observed as exhibited by the absorption spectra in Figure 4c. The absorption for graphene exhibits a rapid reduction going from 300 nm to 400 nm

(UV to visible range) compared to the slow reduction in the absorption for WS_2-graphene. The spectra for WS_2-graphene is more uniform in the wavelength range (300-900 nm) tested. The external quantum efficiency (EQE) of WS_2-graphene/n-Si solar cell in Figure 4d shows a low efficiency (10-20%) in the blue and green spectrum of light and a relatively higher efficiency (~50%) in the near infrared region. The low EQE in the blue end of the light spectrum can be because of the carriers generated close to the front surface being affected by the higher rate of recombination in the front region. The low EQE in the green region can be due to the low diffusion length or high bulk recombination rates that affects the collection probability from the bulk of the solar cell. The higher EQE in the near IR region can be attributed to the ability of charge carriers being generated towards rear end of the device getting transported to the junction.[25]

Utilizing the Van Hove singularity induced absorption peaks in the visual and ultraviolet range of

Figure 4: Photoluminescence spectra for WS$_2$ on (a) graphene/n-Si and on (b) SiO$_2$/Si surfaces. The Lorentzian fits show the neutral exciton (X) and the negatively charged trion (X$^-$) peaks for both the substrates. The PL spectrum for WS$_2$ on graphene/n-Si also exhibits the graphene's 2D Raman peak. (c) Absorption spectra for the WS$_2$-graphene and graphene films showing an increased absorption in the WS$_2$-graphene film in the visible range. (d) External quantum efficiency for the WS$_2$-graphene/n-Si solar cell device.

light, a 4-fold increase in the J_{sc} of the stacked heterostructure (WS$_2$-graphene/n-Si) has been achieved. Thus the deposition of a few layers of WS$_2$ on graphene/n-Si led to (a) an increased light absorption leading to a 4-fold increase in the J_{sc} and (b) an increase in the V_{oc} by 40% due to the introduction of an additional photo-junction. In combination, a 6-fold increase in the solar power conversion efficiency of WS$_2$-graphene/n-Si double-junction photovoltaic cell is found in contrast to the graphene/n-Si single Schottky junction photovoltaic cell.

3. CONCLUSIONS

In this work, we reported the direct-CVD growth of atomically-thin semiconducting WS_2 layers on graphene and obtained a stacked WS_2-graphene/n-Si dual-junction heterostructure. Employing the technique of CVD, we have been able to create a clean interface between WS_2 and graphene avoiding polymer-based chemical transfer process. The CVD approach provides us avenues to control the number of layers of WS_2 and moreover this simple and fast process is also scalable. The stacked heterostructure helped in realizing atomically sharp interfaces. This abrupt change within a few angstrom distances helps in realizing sharp interfaces without inter-diffusion. As a consequence of the atomically thin WS_2-graphene interface and the stronger built-in electric field in the graphene/n-Si junction, the net built-in electric field is towards WS_2. Because of the net electric field, the photo-generated electrons will move toward the n-Si side and the holes toward WS_2 to be eventually collected by the metal electrodes on top. We leveraged the Van Hove singularity induced improved optical absorption of WS_2 in the visible range to enhance the light absorption of the graphene/n-Si device *via* deposition of few layers of WS_2. By synthesizing the stacked heterostructure, we have shown an improvement in the photovoltaic performance of a graphene/n-Si solar cell by depositing few-layers of WS_2 *via* CVD. Hence the improvement in the photovoltaic performance can be attributed to the increased light absorption and the reconfiguration of the energy levels at the WS_2/graphene junction as a consequence of the deposition of WS_2 layers on the graphene/n-Si substrate. The realization of stacked heterojunctions *via* CVD will pave the way for future integrated nanostructures with unique optoelectronic functionalities.

MATERIALS AND METHODS

Synthesis of Graphene on Cu foil *via* Chemical Vapor Deposition: The monolayer graphene samples were prepared *via* chemical vapor deposition (CVD) on a (1"x2") copper foil (25 μm, 99.98% purity) with methane (CH_4, 99.95% purity, Praxair) as the precursor gas and hydrogen (H_2, 99.9999% purity, Praxair) gas as the reducing agent. The wash cycle of copper foil involved

washing with copious amount of water followed by acetone and then isopropyl alcohol. After the first wash the copper foil was immersed in a solution of $Fe(NO_3)_2:HNO_3$ (1M:3M) for 10 minutes to remove native oxide. This was followed by a second wash cycle and then sonication in acetone to remove further ions. The third and final wash cycle was followed by drying with a flow of purified air for 2 minutes. The copper foil was subsequently loaded into a one inch quartz tube on a single heating zone CVD furnace and the reaction chamber was vacuumed to a pressure of 1 militorr (mTorr) in 5 minutes. A steady flow of 100 sccm of H_2 gas was maintained throughout the rest of the synthesis process. After flushing the system with H_2 gas for 10 minutes, the temperature of the furnace was raised to 1050 °C in 15 minutes. This was followed by annealing the Cu foil at 1050 °C for 30 minutes. The reaction was carried out by flowing 10 sccm of CH_4 into the chamber for 1 minute. Subsequently, the CH_4 was turned off and the furnace was opened and allowed to cool down to room temperature quickly.

Transfer of Graphene onto n-Si Substrates: The monolayer graphene produced was transferred to the n-Si substrates using polymethyl-methacrylate (PMMA). The procedure involved spin-coating a 25 mg/ml solution of PMMA (MW 996000, Sigma Aldrich) in anisole (99% purity, Acros Organics) onto the graphene containing Cu foil. This was followed by air drying the PMMA-Gr/Cu foil for 5 minutes and then etching copper by floating the foil in a HNO_3 acid solution (1:3 volume ratio of HNO_3 to deionized water) for 1 hour. The floating PMMA-Graphene was picked up using a quartz substrate and then transferred to a container with deionized water. This process was repeated twice to remove the ions. Eventually the PMMA-graphene samples were picked up using the target n-Si substrates. The PMMA-graphene-Si samples were left to air dry for 1-2 hours. The PMMA removal procedure involved baking the samples on a hot-plate at 60 °C for 20 minutes followed by immersing the sample in a container with acetone. The graphene-Si samples were further washed with acetone to remove any remaining PMMA on the surface.

Photovoltaic Device Fabrications: To prepare the final solar cell devices a lift-off photolithography process was employed. Two out of the ten CVD prepared WS_2-graphene/n-Si samples produced were designed for photovoltaic cell architecture. The graphene-Si and WS_2-graphene/n-Si samples were first spin coated with a photoresist (PR OIR-90612) liquid followed

by exposing it to ultraviolet (UV) light through a mask with our gridded electrode patterns. The samples were then developed by immersing the exposed samples in a developer solution (OPD 4262) for 1 minute which washed away the photoresist from the areas exposed to the UV light. The next step involved depositing the metal electrodes, 10 nm of chromium followed by 50 nm of gold, via electron-beam evaporation. The samples with deposited metals then were washed with acetone to remove metal from the photoresist covered areas leaving behind a gridded electrode pattern. A coating of conducting silver paste was used as the back contact for the solar cell devices.

Raman Spectroscopic Characterizations: The Raman spectroscopy analysis for the samples were done on WITEC-300RA Raman-AFM system using a 532-nm laser excitation source.

Atomic Force Microscopy: The AFM measurements were performed on the WITEC-300RA Raman-AFM system. Tapping mode AFM was performed using silicon tips with a spring constant of 3 N/m and a resonant frequency of 62 kHz.

Photovoltaic Measurements: The photo-electrical measurements on the final devices were performed on a Keithley SMU 2612 source meter using the two-probe method. The photovoltaic effect of the devices were analyzed by measuring the I-V characteristics on the Keithley source meter under irradiation of AM 1.5 illumination from a solar simulator (Sciencetech).

Absorption Spectra and External Quantum Efficiency Measurements: The measurements were performed on the Oriel Cornerstone 130 monochromator system. To measure the absorption percentage, graphene film with and without WS_2 were transferred onto clean quartz slides. Using the monochromator, light from UV and visible range (280-900 nm) was irradiated onto the samples. The intensity of light transmitted through the samples were measured using a photodetector (Newport UV-818). The intensity of transmitted light through an empty quartz slide was used as the base intensity used in calculating the percentage absorption through the graphene and WS_2-graphene samples. The EQE measurement involved irradiating the fabricated device with light of different wavelengths using the monochromator and measuring the corresponding photocurrent through the Keithley SMU 2612 source meter.

AUTHOR INFORMATION

Corresponding Authors

*E-mail: vikasb@uic.edu and sbehura1@uic.edu

Notes

The authors declare no competing financial interest.

REFERENCES

1   A. K. Geim and I. V Grigorieva, *Nature*, 2013, **499**, 419–25.

2   T. Georgiou, R. Jalil, B. D. Belle, L. Britnell, R. V Gorbachev, S. V Morozov, Y.-J. Kim, A. Gholinia, S. J. Haigh, O. Makarovsky, L. Eaves, L. a Ponomarenko, A. K. Geim, K. S. Novoselov and A. Mishchenko, *Nat. Nanotechnol.*, 2013, **8**, 100–3.

3   S. Behura, P. Nguyen, S. Che, R. Debbarma and V. Berry, *J. Am. Chem. Soc.*, 2015, **137**, 13060–13065.

4   R. Debbarma, S. Behura, P. Nguyen, T. S. Sreeprasad and V. Berry, *ACS Appl. Mater. Interfaces*, 2016, **8**, 8721–8727.

5   Y. Wang, Z. Xia, L. Liu, W. Xu, Z. Yuan, Y. Zhang, H. Sirringhaus, Y. Lifshitz, S. T. Lee, Q. Bao and B. Sun, *Adv. Mater.*, 2017, **29**.

6   X. Li, W. Cai, J. An, S. Kim, J. Nah, D. Yang, R. Piner, A. Velamakanni, I. Jung, E. Tutuc, S. K. Banerjee, L. Colombo and R. S. Ruoff, *Science (80-.).*, 2009, **324**, 1312–1314.

7   A. Reina, X. Jia, J. Ho, D. Nezich, H. Son, V. Bulovic, M. S. Dresselhaus and K. Jing, *Nano Lett.*, 2009, **9**, 30–35.

8   S. Bae, H. Kim, Y. Lee, X. Xu, J.-S. Park, Y. Zheng, J. Balakrishnan, T. Lei, H. Ri Kim, Y. Il Song, Y.-J. Kim, K. S. Kim, B. Özyilmaz, J.-H. Ahn, B. H. Hong and S. Iijima, *Nat. Nanotechnol.*, 2010, **5**, 574–578.

9   C. C. Chen, M. Aykol, C. C. Chang, A. F. J. Levi and S. B. Cronin, *Nano Lett.*, 2011, **11**, 1863–1867.

10   Y. Song, X. Li, C. Mackin, X. Zhang, W. Fang, T. Palacios, H. Zhu and J. Kong, *Nano Lett.*, 2015, **15**, 2104–2110.

11   D. Sinha and J. U. Lee, *Nano Lett.*, 2014, **14**, 4660–4664.

12   X. Miao, S. Tongay, M. K. Petterson, K. Berke, A. G. Rinzler, B. R. Appleton and A. F. Hebard, *Nano Lett.*, 2012, **12**, 2745–2750.

13   E. Shi, H. Li, L. Yang, L. Zhang, Z. Li, P. Li, Y. Shang, S. Wu, X. Li, J. Wei, K. Wang, H. Zhu, D. Wu, Y. Fang and A. Cao, *Nano Lett.*, 2013, **13**, 1776–1781.

14   L. Britnell, R. M. Ribeiro, a Eckmann, R. Jalil, B. D. Belle, a Mishchenko, Y.-J. Kim, R. V Gorbachev, T. Georgiou, S. V Morozov, a N. Grigorenko, a K. Geim, C. Casiraghi, a H. Castro Neto and K. S. Novoselov, *Science*, 2013, **340**, 1311–4.

15   V. G. Kravets, A. N. Grigorenko, R. R. Nair, P. Blake, S. Anissimova, K. S. Novoselov and A. K. Geim, *Phys. Rev. B - Condens. Matter Mater. Phys.*, 2010, **81**.

16   M. Bernardi, M. Palummo and J. C. Grossman, *Nano Lett.*, 2013, **13**, 3664–3670.

17   S.-E. Zhu, S. Yuan and G. C. A. M. Janssen, *EPL (Europhysics Lett.*, 2014, **108**, 17007.

18   M. Chhowalla, H. S. Shin, G. Eda, L.-J. Li, K. P. Loh and H. Zhang, *Nat. Chem.*, 2013, **5**, 263–275.

19   A. Kuc, N. Zibouche and T. Heine, *Phys. Rev. B*, 2011, **83**, 245213.

20   C. Lan, C. Li, Y. Yin and Y. Liu, *Nanoscale*, 2015, **7**, 5974–5980.

21   K. M. McCreary, A. T. Hanbicki, G. G. Jernigan, J. C. Culbertson and B. T. Jonker, *Sci. Rep.*, 2016, **6**, 19159.

22   H. R. Gutierrez, N. Perea-Lopez, A. L. Elias, A. Berkdemir, B. Wang, R. Lv, F. Lopez-Urias, V. H. Crespi, H. Terrones and M. Terrones, *Nano Lett.*, 2012, **13**, 3447–3454.

23   T. Yamaguchi, R. Moriya, Y. Inoue, S. Morikawa, S. Masubuchi, K. Watanabe, T. Taniguchi and T. Machida, *Appl. Phys. Lett.*, 2014, **105**.

24   H. Tan, Y. Fan, Y. Rong, B. Porter, C. S. Lau, Y. Zhou, Z. He, S. Wang, H. Bhaskaran and J. H. Warner, *ACS Appl. Mater. Interfaces*, 2016, **8**, 1644–1652.

25   S. Behura, K. C. Chang, Y. Wen, R. Debbarma, P. Nguyen, S. Che, S. Deng, M. R. Seacrist and V. Berry, *IEEE Nanotechnol. Mag.*, 2017, 11, 33–38.

26   A. Berkdemir, H. R. Gutiérrez, A. R. Botello-Méndez, N. Perea-López, A. L. Elías, C.-I. Chia, B. Wang, V. H. Crespi, F. López-Urías, J.-C. Charlier, H. Terrones and M. Terrones, *Sci. Rep.*, 2013, **3**, 1755.

27   L. M. Malard, M. A. Pimenta, G. Dresselhaus and M. S. Dresselhaus, *Phys. Rep.*, 2009.

28   H. Zeng, G. Bin Liu, J. Dai, Y. Yan, B. Zhu, R. He, L. Xie, S. Xu, X. Chen, W. Yao and X. Cui, *Sci. Rep.*, 2013.

29   H. Ago, H. Endo, P. Solís-Fernández, R. Takizawa, Y. Ohta, Y. Fujita, K. Yamamoto and M. Tsuji, *ACS Appl. Mater. Interfaces*, 2015, **7**, 5265–5273.

30   S. Y. Chen, C. Zheng, M. S. Fuhrer and J. Yan, *Nano Lett.*, 2015, **15**, 2526–2532.

31   A. Ferrari and D. Basko, *Nat. Nanotechnol.*, 2013, **8**, 235–46.

32   Q. Wang, T. Soderstrom, K. Omaki, A. Lennon and S. Varlamov, in *Energy Procedia*, 2012, vol. 15, pp. 220–228.

33   X. Li, H. Zhu, K. Wang, A. Cao, J. Wei, C. Li, Y. Jia, Z. Li, X. Li and D. Wu, *Adv. Mater.*, 2010, **22**, 2743–2748.

34   J. M. Shah, Y. Li, T. Gessmann and E. Fred Schubert, *MRS Proc.*, 2003, **798**.

35   A. Kumar and P. K. Ahluwalia, *Phys. B Condens. Matter*, 2012, **407**, 4627–4634.

36   K. Chen, X. Wan, W. Xie, J. Wen, Z. Kang, X. Zeng, H. Chen and J. Xu, *Adv. Mater.*, 2015, **27**, 6431–6437.

37   X. Wan, Y. Xu, H. Guo, K. Shehzad, A. Ali, Y. Liu, J. Yang, D. Dai, C.-T. Lin, L. Liu, H.-C. Cheng, F. Wang, X. Wang, H. Lu, W. Hu, X. Pi, Y. Dan, J. Luo, T. Hasan, X. Duan, X. Li, J. Xu, D. Yang, T. Ren and B. Yu, *npj 2D Mater. Appl.*, 2017, **1**, 4.

38   H. Qiu, T. Xu, Z. Wang, W. Ren, H. Nan, Z. Ni, Q. Chen, S. Yuan, F. Miao, F. Song, G. Long, Y. Shi, L. Sun, J. Wang and X. Wang, *Nat. Commun.*, 2013, **4**, 2642.

39   S. Tongay, J. Suh, C. Ataca, W. Fan, A. Luce, J. S. Kang, J. Liu, C. Ko, R. Raghunathanan, J. Zhou, F. Ogletree, J. Li, J. C. Grossman and J. Wu, *Sci. Rep.*, 2013, **3**, 2657.

40   N. Peimyoo, W. Yang, J. Shang, X. Shen, Y. Wang and T. Yu, *ACS Nano*, 2014, **8**, 11320–11329.

41   T. Kato and T. Kaneko, *ACS Nano*, 2016, **10**, 9687–9694.

42   N. Peimyoo, J. Shang, C. Cong, X. Shen, X. Wu, E. K. L. Yeow and T. Yu, *ACS Nano*, 2013, **7**, 10985–10994.

43   A. Chernikov, T. C. Berkelbach, H. M. Hill, A. Rigosi, Y. Li, O. B. Aslan, D. R. Reichman, M. S. Hybertsen and T. F. Heinz, *Phys. Rev. Lett.*, 2014, **113**.

44   B. Zhu, X. Chen and X. Cui, *Sci. Rep.*, 2015, **5**, 9218.

45   A. A. Mitioglu, P. Plochocka, J. N. Jadczak, W. Escoffier, G. L. J. A. Rikken, L. Kulyuk and D. K. Maude, *Phys. Rev. B - Condens. Matter Mater. Phys.*, 2013, **88**.

46   K. F. Mak, K. He, C. Lee, G. H. Lee, J. Hone, T. F. Heinz and J. Shan, *Nat. Mater.*, 2012, **12**, 207–211.

47   U. Dutta and P. Chatterjee, *J. Appl. Phys.*, 2004, **96**, 2261–2271.

48   T. K. Todorov, T. Gershon, O. Gunawan, C. Sturdevant and S. Guha, *Appl. Phys. Lett.*, 2014, **105**, 173902.

49   A. Hadipour, B. De Boer and P. W. M. Blom, *Adv. Funct. Mater.*, 2008, **18**, 169–181.

50   I. Mathews, D. O'Mahony, B. Corbett and A. P. Morrison, *Opt. Express*, 2012, **20**, A754.

51   Y. Zou, Z. Deng, W. J. Potscavage, M. Hirade, Y. Zheng and C. Adachi, *Appl. Phys. Lett.*,
        2012, **100**.
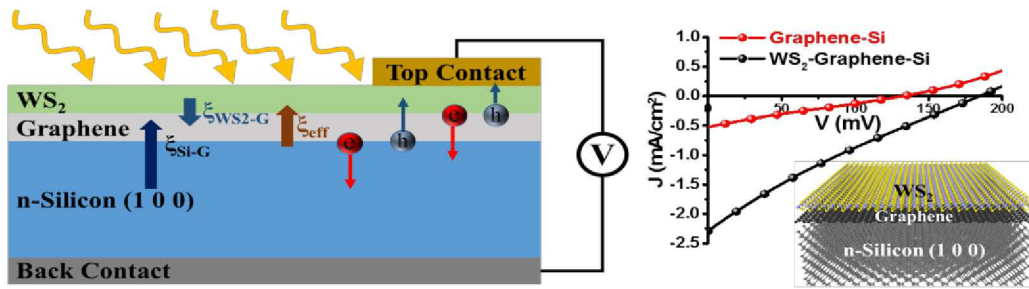
By leveraging the Van Hove singularity induced enhancement in optical absorption, a photovoltaic cell is designed with WS$_2$ on graphene atop n-Si to enhance the power conversion efficiency.